Automated fabrication of hybrid printed electronic circuits

Ulrich Gengenbach*, Martin Ungerer, Liane Koker, Klaus-Martin Reichert, Peter Stiller, Stephan Allgeier, Bernd Köhler, Xiaoqi Zhu, Chengyuan Huang, Veit Hagenmeyer

Institute for Automation and Applied Informatics, Karlsruhe Institute of Technology, Karlsruhe 76021, Germany

ABSTRACT

Printed electronics offer great potential for new applications such as Internet of Things devices and wearables. However, to date, only a limited number of electronic functions and integration densities can be realised by printing processes. Hence, hybrid printed electronic circuits are actually created by mounting silicon electronic components. Since both printed materials and processes are continuously evolving, an accompanying structured development methodology is required. This paper highlights a digital workflow from design to automated fabrication using the example of a demonstrator circuit. A multi-layer vector ink-jet printing process to print electronic devices onto foil substrates with three functional inks is presented. This printing process is improved using a newly set-up printing system: Integrating a piezo print head into the path planning of the printing system and its control as a virtual stepper axis enable highly precise vector printing. This leads to printed resistors with low tolerances. Adaptations of surface mount technology for assembling silicon electronic components onto printed foil substrates are discussed. Finally, image processing methods to cope with deformations of the flexible foil substrates in the fabrication process are introduced.

1. Introduction

Printed electronics holds the potential to fabricate flexible, low cost electronic devices and systems to realise new applications such as wearables, Internet of Things (IoT) devices and sensors [1-3]. The low material consumption due to the additive nature of the process complies with the trend towards resource efficiency.

The key component of printed electronics are functional inks based on novel nanomaterials. The ink portfolio is continuously growing, ranging from materials for printing conductors, passive components (e.g. resistors, capacitors), and active components (e.g. diodes, transistors) [4,5]. Established printing techniques such as offset printing, screen printing or ink-jet printing [6] have been adapted for functional printing [7,8]. New printing techniques such as aerosol-jet printing and electrohydrodynamic ink-jet printing have specifically been developed for functional printing applications [9]. This growing number of printing techniques allows good scalability from digital processes such as ink-jet or aerosol-jet printing for small numbers of piece-parts to high-throughput production by for example roll-to-roll (R2R) screen-printing. After the ink has been deposited on the substrate by the printing process, one or more postprocessing steps such as drying, curing and sintering are required to yield the desired functional layer on the substrate. Depending on the complexity of the circuit, the sequence of printing and

postprocessing is repeated several times with different functional materials.

The benefits of printed electronics come, however, at the price of a few challenges. The performance of printed components is frequently substantially lower than that of silicon components. For example, the conductivity of printed silver conductor tracks is lower than bulk silver by a factor of two or more; switching frequencies of printed transistors are in the low MHz range, while silicon transistors easily reach GHz levels [2]. In addition, complexity and integration density of printed circuits are also orders of magnitude lower than current integrated silicon circuits, implying that a printed microcontroller, for example, cannot be expected in the near future [1]. Progress in silicon electronics has been significantly fostered by industry.

For decades, companies and research institutions have cooperatively developed and standardised silicon electronics materials, design methodologies, processes and equipment. These activities have led to tremendous technological progress, given rise to new industries and have made new products available to the consumer [10]. Compared to this state of the art of silicon electronics, printed electronics is still in its infancy. Hence, in the field of printed electronics research, questions and challenges exist along the entire development and fabrication chain. To start with, functional printing is still lacking the design infrastructure (e.g. design rules, process design kits) established in classic electronic fabrication. First rule sets and tools are under development but there is still a long way to go [2,11]. In semiconductor fabrication,

structure size is primarily defined by lithography. In functional printing, structure size, e.g. line width depends on the interaction between ink and substrate, i.e. the wetting properties of the substrate for a given ink. Moreover, in piezo ink-jet printing the structure size on the substrate depends on the droplet diameter generated by the print head. The droplet diameter is determined by the printing nozzle diameter and by the piezo actuation waveform [12]. Thus, in functional printing, structure size depends on the interactions between printing system, ink and substrate. Finally, as printed electronics is still a technology in ramp-up phase, materials properties and their reproducibility frequently remain an issue affecting process yield and product quality. Furthermore, ink properties may vary from batch to batch. Thermal stability of substrates puts constraints on postprocessing steps and limits geometric fidelity of printed structures. Substrate suppliers optimise the substrate surface for structural definition by chemical functionalisation and in some cases additionally by nano-structuring of the substrate surface [13]. For low temperature substrates, suppliers offer heat stabilised foils. This does, however, not exclude anisotropic elongation, shrinkage or even warpage during processing. These effects must be detected and considered in the fabrication process.

Hence, in order to reap the above-mentioned benefits of printed electronics, a substantial effort is involved in investigating printing parameters and ink substrate interaction [13]. Moreover, in order to take advantage of the adaptability of flexible electronics, printed device performance under flexural strain has to be taken into account [14].

A pragmatic approach in realizing printed circuits despite these challenges is to decide which components are reasonable candidates for printing, then to select the respective materials, establish the relevant printing processes and gradually establish the complete fabrication flow to ultimately realise the comprehensive circuit. Functional elements that cannot yet be realised by functional printing are mounted by adapted surface mounting processes (e.g. by adhesive bonding of surface-mounted devices (SMD)) onto the printed substrate yielding hybrid printed electronic circuits [9]. The present paper highlights a new methodical approach using a fully digital design and fabrication workflow from design to ink-jet printing and component mounting outlined in [15] in greater detail.

To this end, the remainder of the present paper is organised as follows: In Section 2, the applied materials and methods are introduced, including equipment used as well as design, fabrication and measurement set-ups. In Section 3, the theoretical basis for the novel control of the vector ink-jet printing process is represented. In Section 4, the results regarding the advances of the design and fabrication workflow are outlined, discussed and a printed, hybrid integrated demonstrator circuit is presented. Finally, a conclusion is given, including an outlook and challenges to be addressed in future research.

2. Materials and methods

In the following, the materials and methods used to realise the automated fabrication of hybrid printed electronics are introduced.

2.1. Materials

2.1.1. Inks

The wiring, contact pads, capacitor base, top plates and fiducial marks are printed with the nanoparticle silver ink Advanced Nano Products DGP 40LT-15C; the resistors with the carbon ink Methode Electronics Ink 3804. The capacitor dielectric and the cross-connect insulation are realised using a Barium-Strontium-Titanate (BST) ink developed at KIT [16].

2.1.2. Adhesive

The conductive adhesive to contact the electronic components to the substrate is the two-component adhesive Elecolit 325 by Panacol with a mixing ratio of 1:1 filled with silver particles with a size of 25 μm.

To improve the mechanical fixation of the SMD components, the non-conductive structural adhesive Loctite 3094 is additionally applied.

2.1.3. SMD components

The tetrode Infineon BF2040 in a SMD SOT143 package is used for realisation of the transistor function by hybrid integration.

2.1.4. Substrates

Two Polyetheylentherephthalate (PET) foil substrates, Dupont Melinex ST 506 and Mitsubishi Paper Mills NB-TP-3GU100 are used. The Melinex substrate has a thickness of 125 μm, a clear reflective surface and is modified by a chemical process for improved printability. The other PET substrate, NB-TP-3GU100 by Mitsubishi Paper Mills, is a 135 μm thick flexible PET substrate with a nano-porous top layer for improved printability. Due to this layer conductive structures can be achieved with the silver nano-particle ink without thermal postprocessing.

2.2. Methods

2.2.1. Workflow

Fig. 1 illustrates the digital workflow. The data flow goes in the vertical direction starting with circuit development, layout definition in the computer aided design (CAD) system Altium and fabrication programme generation in the generator tool. The fabrication flow is depicted in the horizontal from printing over inspection to SMD component mounting.

2.2.2. Circuit design and automatic generation of fabrication programs

The circuit and the derived PCB layout are designed with the CAD software Altium version 14.1.5. The design space is defined by the polymer substrate size of 150 mm x 150 mm. The CAD design of the circuit is the basis for all steps of the fabrication workflow. Circuit elements are allocated to different CAD layers according to their function in order to be able to assign separate properties to them for the subsequent processing steps. Moreover, component position, orientation and package types are included in the layout. The objective is to derive as many data as possible for subsequent steps from this base information. The industry standard for exchange of layout data ODB++ is chosen to export the CAD data from the Altium CAD system [17]. By means of a generator tool developed in Python control programs for the processing stations printing and SMD component mounting as well as a template for quality control with image processing are derived from the CAD layout. The tool imports the ODB++ files of the different CAD layers and builds an internal data model of the circuit from these data. After verification and cleaning this data model leads to two weighted graphs, one for one-dimensional features (conductor tracks) and one for two-dimensional features (e.g. pads, capacitor plates) [18]. Generation of tool paths for machining tasks is a problem typically tackled by graph traversal algorithms [19]. Tool paths can be subdivided into machining paths where the tool interacts with the workpiece and empty runs where the tool is moved from one machining site on the workpiece to the next. It is evident that empty runs are unproductive auxiliary process time and thus have to be kept as short as possible. Hence, the main optimisation criterion is the reduction of empty runs, as this directly reduces overall machining time and thus cost. This NP-hard optimisation task is treated as travelling salesman problem, for which no optimal but a number of effective algorithms exist [20]. For generation of optimised toolpaths for one-dimensional features i.e. the conductor tracks of the circuit a nearest neighbour algorithm [18,21] and an ant colony algorithm [22,23] have been implemented in Python.

2.2.3. Vector ink-jet printing

A custom-built print head motion system is used for ink-jet vector printing (Fig. 2). The system basis is a Newport optical table (RS 1000) mounted on Newport SLM-6A legs to damp potential environmental vibrations. The motion system consists of an OWIS Limes 170–400 HSM
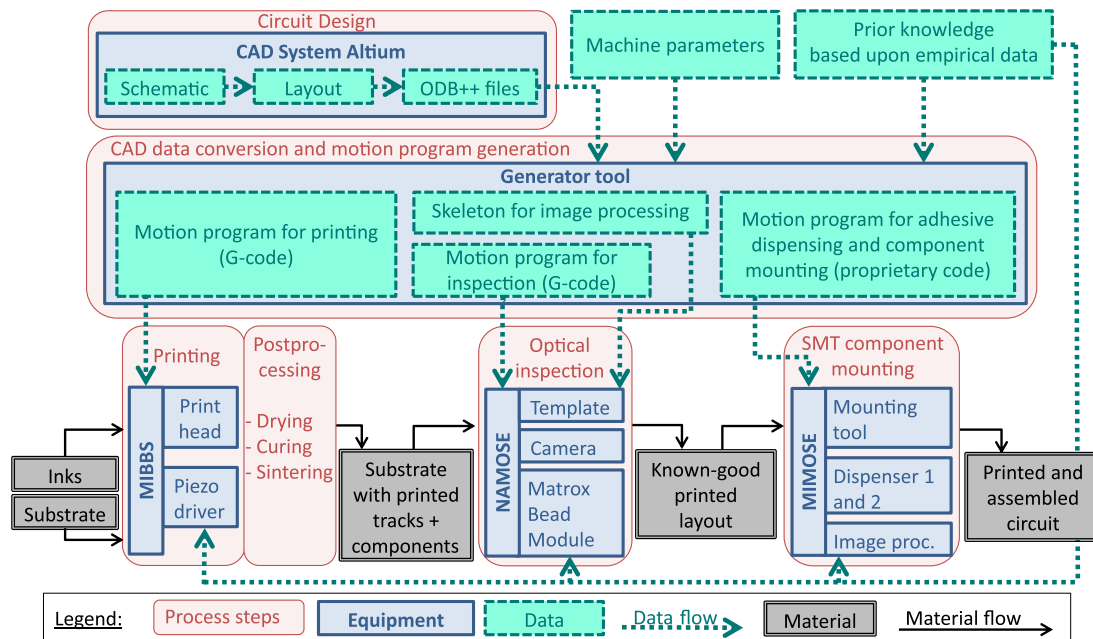
Fig. 1. Digital workflow from design to code generation and ink-jet printing and component mounting.

precision stage with 400 mm stroke and ±3 μm repeatability mounted to the optical table as an x-axis. Above the x-axis, a gantry built with OWIS SYS 65 profiles is mounted carrying the same axis type as the y-axis. On top of the y-axis, an OWIS Limes 60–100 HSM precision stage is mounted as a z-axis with a stroke of 105 mm and ±2 μm repeatability.

All three stages are driven by ball screws with two-phase stepper motors. The motion control is realised by means of a Beckhoff CX2040 industrial PC running Windows 7 and TwinCAT 3 PLC with the PTP and NCI modules. The Beckhoff NCI module allows path control (linear, circular) and motion programming in G-Code (ISO 6983). The stepper motors of the three precision stages are connected to the CX2040 controller by Beckhoff EL7047 stepper motor terminals (SMT).

The single-nozzle Microfab print head (MJ-AL-01–50–8MX) is mounted to the z-axis. It is controlled by the MicroFab Jet Drive III piezo controller and a vacuum controller. Piezo parameters and droplet formation are controlled by the MicroFab Jetserver software running on a Windows PC. It allows waveform parameters to be adjusted and visual observation of droplet formation using a camera and a strobo-scope. The jetting frequency can either be set for continuous jetting in a frequency range from 0 to 20 kHz or by initiating single shots from an external +5 V trigger signal. An integrated image processing system (ADCIS Aphelion) is used to monitor droplet formation, droplet velocity and droplet volume from images acquired by a drop watcher camera. The substrates to be printed are clamped on a vacuum chuck mounted onto the x-axis. As substrate temperature is an important parameter for controlling ink spreading and thus printing precision, the vacuum chuck can be heated up to 200 °C.

2.2.4. Adaptation of smd component mounting

In addition to printing structures and components, the automated workflow includes mounting of discrete electronic components onto the printed circuit. This hybrid set-up serves two purposes. First, as outlined in Section 2.2.6, in the development phase devices realised by mounted SMD components can be step by step replaced by printed electronic components. The functionality of each kind of printed components can thus be tested within the circuit. The second purpose of the mounting process is the integration of complementary silicon components that cannot yet be realised by functional printing.

SMD component mounting on rigid thermally stable printed circuit boards (PCBs) is a standard process established for decades [24-26].

This component mounting technology can be adapted to thermally less stable, flexible foil substrates. The lower thermal stability implies that standard PCB soldering processes are not applicable. While conductive adhesive bonding offers a viable, low temperature alternative, mounting a rigid SMD component or bare die on printed contact pads on a flexible substrate poses a few challenges:

(1) The adhesion of a printed contact pad on a polymer foil substrate is comparatively weak. According to [27] the dominating effect binding nano-particles to a planar polymer surface such as the Dupont Melinex ST 506 are van-der-Waals forces increased by nano-indentation.

For a polymer substrate with a nano-structured surface such as the Mitsubishi Paper Mills NB-TP-3GU100, a mechanical inter-locking between the nano-particle layer and the porous surface can be observed [13]. Still, this interlocking does not result in a strong adhesion comparable with copper layers on a conventional PCB.

(2) If the flexibility of the foil substrate is required by the application of the printed system, the mounted component is likely to peel off when foil bending occurs in its vicinity. Hence, the interface between the rigid component and the flexible foil has to be made robust against this additional strain.

(3) In conventional electronics self-centring of components due to surface minimisation of molten solder supports component alignment on the PCB [26,28]. This effect is not applicable when mounting components with conductive adhesive on printed foils. Thus, component placement has to be more precise also taking into account substrate deformations due to the thermal processes as outlined in Section 2.2.5.

In conventional electronics, the mechanical fixation of a flip-chip on a PCB does not rely on the mechanical properties of the electrical connection (solder or conductive adhesive) alone. In cases where excessive strain of the connection is to be expected due to, e.g., thermal strain or vibrations [26], a function separation of the PCB/flip-chip connection is achieved by:

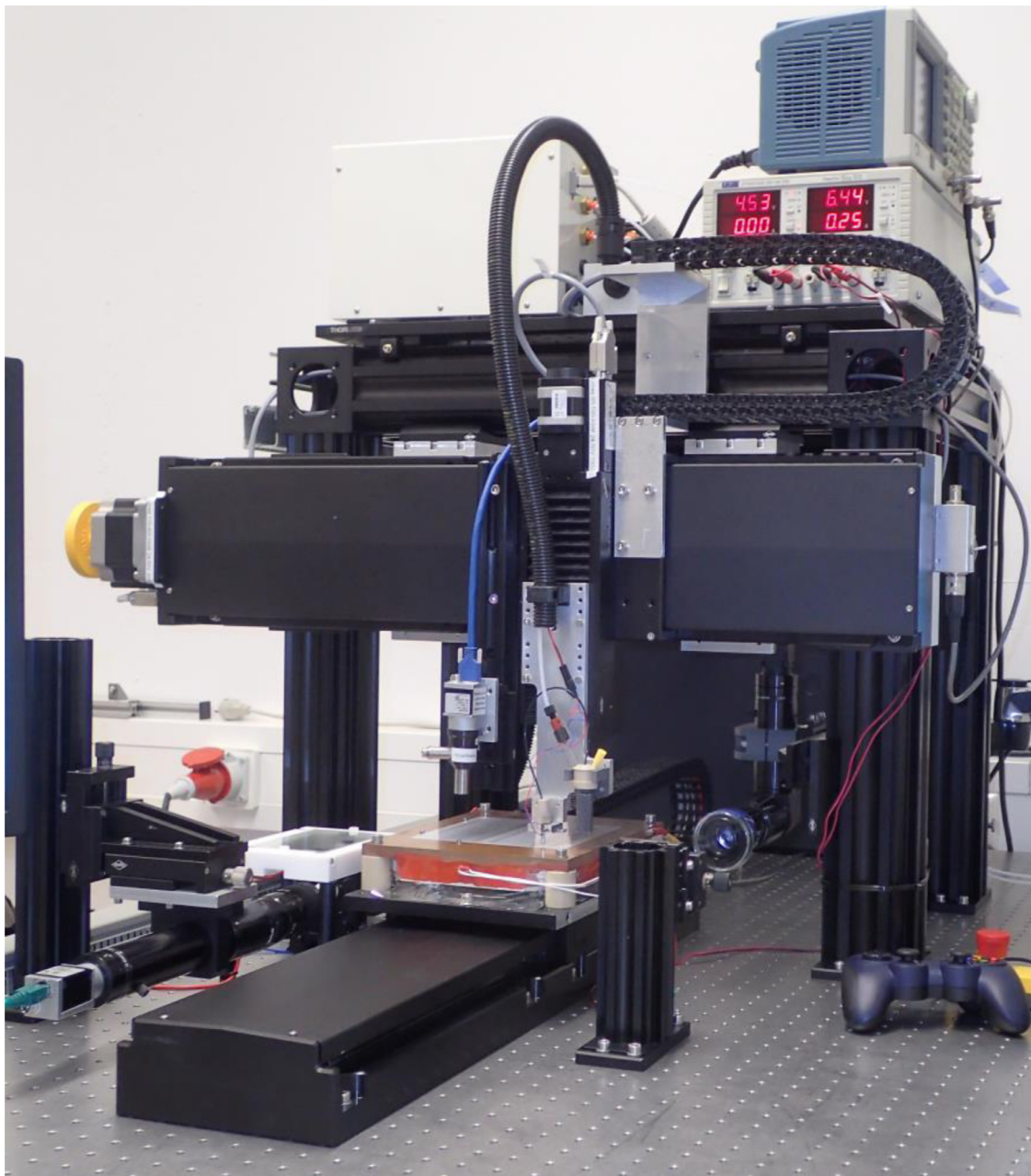- electrical connection: Solder or conductive adhesive between flip-chip and PCB bond pads

Fig. 2. The custom-built vector printing system MIBBS2 [15].

- mechanical fixation: Underfiller, an adhesive that builds an additional mechanical joint between the silicon die and the PCB [26]

A similar principle can be used to alleviate the first and address the second challenge by creating an additional mechanical joint between SMD component/bare die and printed foil with a structural adhesive. But unlike the underfiller, the structural adhesive is applied before the component is placed. Shear tests of SMD components mounted onto PET foils with this principle confirmed that the mechanical fixation is increased significantly [29]. Still, the electrical connection might be weak due to poor adhesion of the printed bond pad on the foil substrate. This situation can be improved by just the opposite strategy than above, by function integration. The prerequisite is however, that not the entire bond pad surface is required for transfer of the electrical power. If this is the case, the bond pad shape can be redesigned in such a way that it yields both an electrical connection with its metal coated area and a mechanical connection with the plain substrate area.

The SMD components are assembled with the four-axis Cartesian handling platform MIMOSE [30] (Fig. 3). Substrate fiducial mark position is acquired with top camera Basler acA1920–25uc with a resolution of 1920 px × 1080 px and a variable field of view. Furthermore, the bottom camera Basler acA 1300–200uc in combination with a TZ3–2X-32-MA objective and a right-angle adaptor with a resolution of 1280 px × 1024 px and a field of view of 3.2 mm × 2.4 mm are used for component inspection from below. The foil substrate is clamped on the xy-stage by a vacuum chuck. The substrate has printed fiducial marks for substrate alignment at the four corners. The MIMOSE is further equipped with a vacuum gripper tool and two pressure time dispensers. The control software of the MIMOSE is from LPKF Motion Systems and can be accessed by a C/C++-API. The two cameras are read out via the software Pylon supplied by the manufacturer Basler. Acquired images are processed with C++ programs based on OpenCV. An in-house image
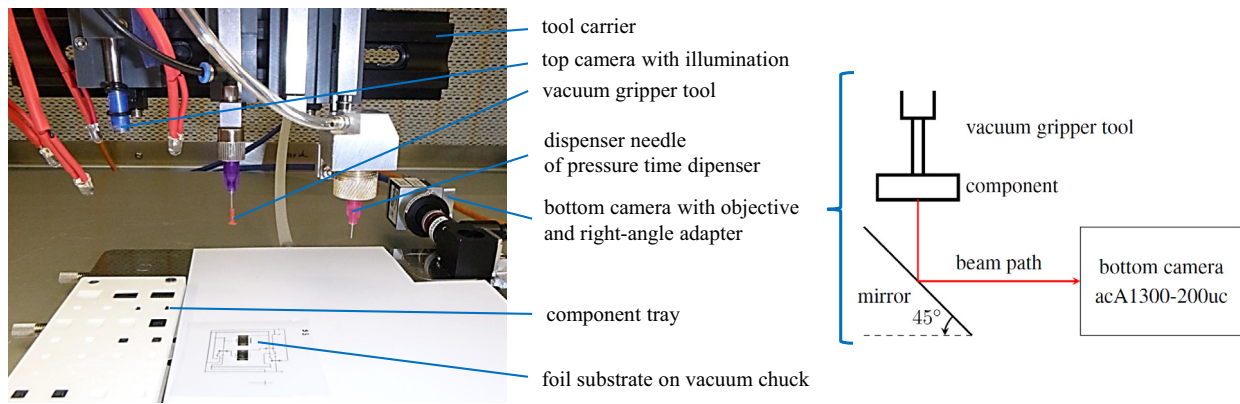
Fig. 3. MIMOSE assembly machine and schematic optical path of the MIMOSE bottom camera.

processing software tool is applied for development and calibration purposes.

2.2.5. Image processing for substrate deformation characterisation and defect detection

Under thermal treatment e.g. nanoparticle sintering at 120 °C, the PET substrates exhibit a deformation behaviour, shrinkage and warpage that has to be taken into account in the fabrication process. Manufacturers claim isotropic substrate shrinkage of e.g. 0.15% at 120 °C for the Melinex ST 506 foil. It was however observed in our experiments, that in reality the deformation is strongly anisotropic after the thermal treatment in our process chain. A possible explanation are the mechanical strains that are embedded in the foil by the roll-to-roll fabrication process, the strains in rolling direction being higher than transversely.

In order to face the challenge of the substrate deformations, a systematic evaluation of the deformation behaviour is being performed for every process inducing thermal load on the substrates. The evaluation is divided into two steps: the analysis of deformation in the x-y-plane (shrinkage) and a warpage analysis.

2.2.5.1. Detection of shrinkage.
During printing as well as during component mounting the substrate is planarised by the vacuum chuck of the respective process station. Thus, during processing, the deformation in the x-y-plane is most relevant. In order to investigate this shrinkage, a matrix of fiducial marks is applied to the substrate. Positional deviations of these fiducial marks are evaluated by image processing after every thermal process step. As a first step, deformation of empty substrates under thermal load is investigated.

2.2.5.2. Detection of warpage.
Strong warpage of the substrate may lead to mechanical strain in the printed structures and in the interconnection of the assembled parts after the release of the vacuum clamping. Moreover, it might even cause height variations of the substrate during the processing steps, despite the vacuum clamping. If further structures are printed onto the substrate after sintering, those height variations have to be determined and compensated, in order to ensure a constant distance between substrate and print head.

In order to measure the substrate surface topography, a deflectometric measurement process is being developed. The set-up exploits the reflective surface characteristic of the foil substrates. The measurement principle is shown in Fig. 4. The substrate to be analysed is used as a mirror. A camera and a pattern generator (e.g. a computer screen) are positioned so that the light emitted from the pattern generator is reflected by the surface of the substrate into the camera. The surface area under test has to be captured by the field of view of the camera. The measurement process uses a series of specific patterns that encode the screen location p in x- and y-direction [31]. From the recorded image sequence, a map of correspondences between camera pixels c and the corresponding screen
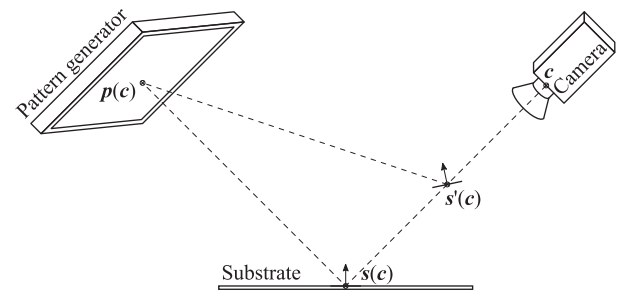

Fig. 4. Deflectometric measurement principle (adapted from [34]).

locations $p(c)$ can be calculated. Given that the position of the camera is known in relation to the pattern generator, these correspondences infer information on the surface under test (more precisely on its normal vector) by tracing the view rays of the camera pixels. This information is ambiguous for a single-camera set-up; for example two different view ray paths for a camera pixel c with reflections at potential surface points $s(c)$ and $s'(c)$, respectively, are illustrated in Fig. 4. Several approaches have been proposed to circumvent this ambiguity [31]. One possible solution is stereo-deflectometry which introduces a second camera into the set-up [32]. In essence, every camera measures a field of potential normal vectors in the 3D measurement space. For a stereo-camera set-up, the two measured normal vector fields coincide at actual surface points (e.g. $s(c)$) and differ everywhere else (e.g. $s'(c)$). This information is used to reconstruct the surface under test. It should be noted that, for non-opaque substrate materials, a fraction of the light emitted by the pattern generator will enter the substrate, will be reflected at the back surface, and interfere with the front surface reflection signal [33]. Considering the similarity of both partial signals due to the small thickness of the substrates used (125 μm), the effect of the backside reflection on the measurement is neglected.

2.2.5.3. Optical inspection of printed structures.
After every printing and postprocessing step the substrate is automatically inspected by means of an image processing system [18] (Fig. 1). The measurement plan for the inspection system is also derived from the layout by the generator tool. Based on the Bead Module of the Matrox Imaging Library the inspection software measures track width and detects gaps. A gap means that droplets are completely missing leading to an interruption of the track. This yields the circuit non-functional and hence to discard of the printed structure. A local, lower track width will increase track resistance, but the circuit may still be functional. Hence, in order to improve yield, circuits where track widths below 50% of the nominal track width are detected are marked for visual inspection by an operator and subsequent decision to discard or keep in the process chain.
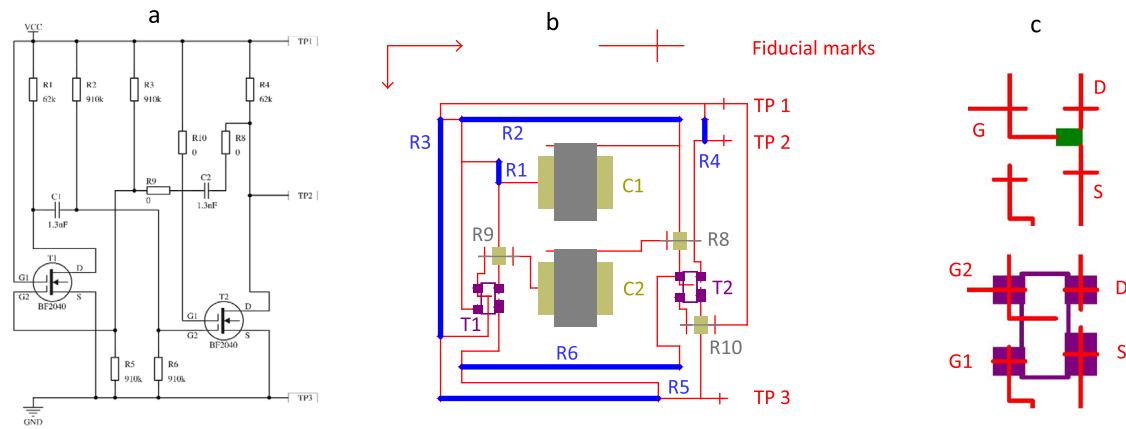
Fig. 5. Demonstrator circuit (a) schematic (b) layout for printing (c) iterative design for transistor to be printed (top) and to be assembled with SMD component BF2040 (bottom).

2.2.6. Iterative design of the demonstrator circuit

The iterative design approach describes a step-by-step realisation of a fully printed circuit. Thereby, structured testing and, if necessary, optimization are performed in every realisation step. In the following, this approach is introduced by using the example of a demonstrator circuit, an astable multivibrator. The circuit is composed of six resistors, two capacitors and two transistors, and its output is an oscillating voltage [35]. The schematic of the demonstrator circuit is shown in Fig. 5(a), including the desired resistive and capacitive values. The iterative design starts with circuit simulations with the LT-Spice software. Thereby, parasitic resistances of conductive tracks and printed capacitors are modelled as additional resistors. Additionally, the circuit is simulated as fully printed setup as well as with mounted SMD transistors. The results show, that with a supply voltage of 1.5 V, the circuit output with a frequency of ca. 425 Hz can be used to drive a piezo buzzer [35]. In parallel a first test vehicle based on a printed circuit board (PCB) with mounted SMD components is set up. This first physical model also takes peculiarities of the printed circuit into account, e.g. parasitic resistances of the conductive tracks and the capacitors, by including additional resistors. Then the printed passives are characterised separately. In the next versions of the PCB test vehicles the printed passives are gradually mounted on the PCB and tested in the circuit. Moreover the conductive tracks are printed onto a foil substrate, all other circuit devices are mounted as SMD components and this circuit is also tested [18]. When the function of the individual printed components has been verified in this way ultimately they are combined in a comprehensive layout and process chain to print the full circuit. The main challenge is the printing of active components, particularly the transistors. The circuit is therefore designed to be modular, allowing transistors to be printed directly into the circuit or discrete devices to be mounted onto the foil substrate (SMD transistors or printed transistors [29] on a separate substrate). The same design and testing philosophy is applied for the cross-connects. These can either be printed directly or realised by mounting discrete components (SMD zero Ohm resistors). In the printing layout presented in Fig. 5(b), all passive components including conductive tracks, resistors, capacitors and cross-connects are printed. Every layer colour indicates either a specific ink type being printed to realise a specific functionality (e.g. red: wiring, blue: resistors) or a mounted component. These layer colours mainly reflect the different layers used in the Altium CAD software to address the different functionalities. The only exception are the fiducial marks that are placed on a separate layer in Altium to facilitate fiducial mark acquisition and positioning of the substrates during the fabrication process steps. Due to the iterative design, the cross-connects R7, R8 and R 9 and the transistors T1 and T2 comprised in the schematic can either be assembled with SMD zero Ohm resistors and tetrodes BF2040 or realised by printed components. The layout allows for both approaches

by integrating contact pads for SMD components as well as contacts for printed cross-connects and transistors. In Fig. 5(c), this iterative design approach is visualised using the example of the printed (top) or assembled (bottom) transistor.

Several approaches exist for adapting the properties of printed resistors. Jung et al. adapt resistance by altering ink properties and by printing multiple layers while keeping the geometry (line length) of the printed resistor constant [36]. Our approach uses the line length as governing parameter while keeping resistance per printed length unit constant. A carbon resistor ink with constant ink properties is printed in a single layer using a novel vector printing process. Thus, in the layout in Fig. 5(b), two different line lengths (blue) are designed to realise two resistive values. The capacitor is realised as a three-layer plate capacitor setup: two silver plate electrodes at top and bottom and a BST dielectric in the middle. The effective capacitive area is $4 \times 4 \, \text{mm}^2$. The target capacitance is 1.3 nF. The variations of capacitance are still relatively high, resulting partly from variations in ink composition, area, thickness and uniformity of the printed dielectric. Moreover since the printed capacitors are not packaged, in operation, capacitance is sensitive to ambient humidity. All of these influences are being investigated and addressed in current research [37-39].

The mounted tetrode Infineon BF2040 in a SMD SOT143 package allows the properties of the printed transistor to be emulated as closely as possible. The next step towards a fully printed circuit can be taken by printing the transistors between the Gate (G), Drain (D) and Source (S) contacts as shown in the top part of Fig. 5(c). While the output of the multivibrator circuit was two LEDs blinking at a single digit Hertz frequency [18] in the first version with printed tracks and mounted SMD components, the present circuit is adapted to the device parameters of capacitors [16] and transistors currently printed at KIT.

This final demonstrator circuit yields an output of several hundred Hertz that is made clearly audible by the piezo buzzer driven by the circuit.

In the course of the enhancement of the design, the cross-shaped fiducial marks shown in Figs. 5 and 6 are enhanced to circular fiducial marks containing a cross in the centre to optimise positioning based on image processing.

2.2.7. Fabrication process

In Fig. 6, the fabrication process for the demonstrator is visualised both as flow diagram (left side) and as layer structure of the circuit growing from top to bottom (right side). The process sequence consists of four different printing processes, each including postprocessing (drying or UV-curing) and optical inspection, as well finally a SMD component mounting process.
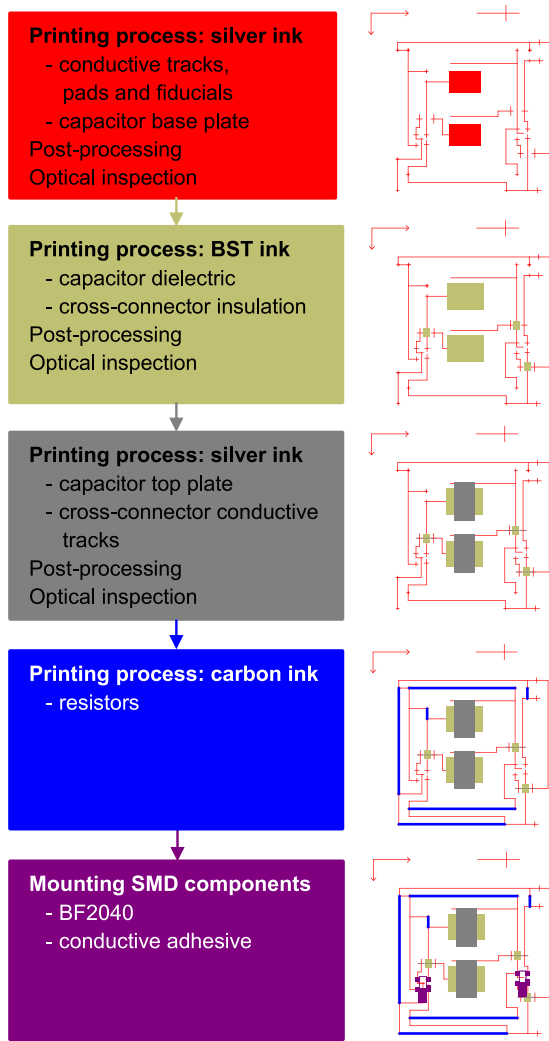
Fig. 6. Fabrication process of the demonstrator circuit composed of four printing steps and discrete component mounting (adapted from [15]).

3. Calculations

Fine-grained control of droplet overlap on the substrate is a requirement for obtaining reproducible properties for printed functional structures [40]. In the case of conductive tracks or resistors, for nanoparticle inks in addition to base material conductivity and postprocessing conditions (e.g. sintering), constant droplet spacing is the key parameter that determines resistance. Thus, by means of a precisely controlled droplet spacing over the entire line length, high-precision resistors can be printed directly. For a vector ink-jet printed capacitor, droplet overlap and line spacing are process parameters that influence the thickness of the dielectric layer and thus capacitance. A novel strategy for integrating control of the piezo print head shooting frequency into the path planning of a motion system is introduced in the following.

$$v_s(t) = f_s(t)l_{step} \qquad (1)$$

$$v_p(t) = f_p(t)d_{dot} \qquad (2)$$

In Eq. (1), the motion velocity $v_s(t)$ of a stepper axis depends on the constant length per step increment l_{step} (µm) and the variable stepper pulse frequency $f_s(t)$ (Hz). Integrating Eq. (1) over time yields the motion path of the axis. In vector printing a line is a concatenation of single dots. Thus, a line printing velocity $v_p(t)$ can be written as the product

of the constant dot offset d_{dot} (µm) and the variable piezo shooting frequency $f_p(t)$ (Hz) in Eq. (2). Thereby, the parameter d_{dot} is an empirical constant used to set the overlap between consecutive dots. The choice of d_{dot} depends on the functional requirements of the printed line.

A low d_{dot} e.g. 25% of the dot diameter will yield a high overlap between dots, with uniform line width and good conductivity. A high d_{dot}, for example, 80% of the dot diameter on the other hand will result in a line of dots barely touching each other and a more "wavy" line contour [40]. In this case, the conductivity will be lower and less uniform over line length, but ink consumption and processing time will also be reduced. A low d_{dot} is recommended to enable highly reproducible printing of resistors. The print head is positioned by the handling system. Printing with a constant piezo frequency would lead to ink accumulation in the acceleration and deceleration phases of print head motion. To obtain uniform drop spacing, the print head shooting frequency has to be adjusted to the axis velocity. It is evident that the two velocities (1) and (2) are conceptually equivalent, which means that the piezo print head can be regarded as a virtual stepper axis. Following the same reasoning, the real stepper axis parameter "maximum velocity" has an equivalent maximum line printing velocity depending on the "maximum jetter frequency" f_{pmax}. This parameter needs to be experimentally determined for every combination of ink and print head. The other stepper axis parameters "acceleration" and "jerk" have no physical equivalent for the piezo print head. These values can therefore be set to arbitrarily high values beyond the maximum values of a real stepper axes, so that they are not constraining.

4. Results and discussion

The digital workflow outlined in Section 2.2.1 is enhanced both, with respect to data processing and with respect to the fabrication processes. The effects of these enhancements are assessed with test structures and a demonstrator circuit.

4.1. Vector toolpath generation for single nozzle piezo ink-jet printing

The wiring of six demonstrator circuits on a substrate resulting in a graph with 254 nodes for the algorithms to consider is used as benchmark to compare the performance of the two tool path generation algorithms (nearest neighbour and ant colony). Both are implemented in Python and the benchmarks are run under Ubuntu 16.04 Linux on a single core of an Intel (R) Core (TM) i7–7700 at 3.6 GHz. Using arbitrary starting points, the nearest neighbour algorithm is run 1012 times, while the ant colony algorithm was run with different sizes of ant colonies (10, 20, 30, ..., 250) 2134 times in total.

Table 1 outlines the performance of the two algorithms. The ant colony algorithm running with a small colony size of only ten ants achieves worse results than the nearest neighbour algorithm at an increase of computation time by a factor of 80. Best performance, a 4% reduction of empty run length, of the ant colony algorithm is obtained with a colony size of 70 ants. The computing time increased however by a factor of 3750. This increase is substantial; it may however be worthwhile as computing time is way less expensive than machining costs. Moreover, this computing time is a one-off cost while the reduction of machining costs is realised for every printed foil substrate.

### 4.2. Improvement of line printing quality with the virtual stepper axis

Operating the MicroFab piezo print head with fixed jetting frequency leads to droplet accumulation during acceleration and deceleration phases of the print head motion system. In order to make this visible and quantifiable the printing parameters are modified in such a way that the dots do not overlap but rather form a dotted line. With proper print head frequency and velocity the droplet spacing should be constant along printed lines. Printed dotted lines are imaged with a computer controlled microscope Leica INM 200 with a field of view

Table 1
Comparison of tool path generation algorithms.

	Nearest neighbour	Ant colony (10 ants)	Ant colony (70 ants)
Number of runs of algorithm	1012	87	31
Length of empty runs (mm)			
Minimum	1265	1255	1194
Maximum	1398	1722	1288
Mean	1328	1355	1232
Computation time (CPU seconds)	2	170	7500
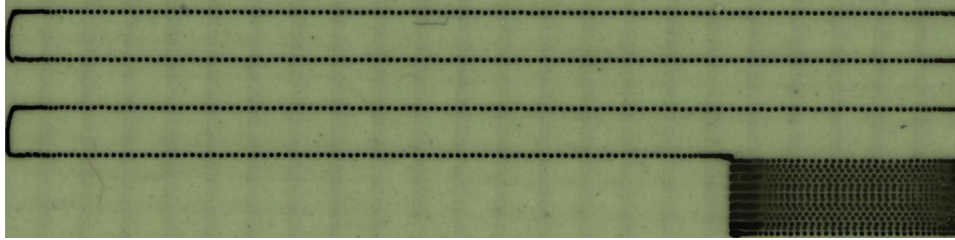
Fig. 7. Contact pad and meander of conductor tracks printed with fixed jetting frequency and increased droplet spacing to visualise ink accumulation in acceleration and deceleration phases.
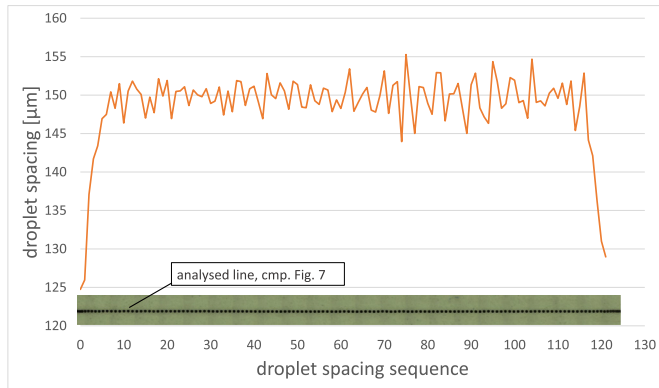
Fig. 8. Droplet spacing along one line of the meander in the region where distinct droplets can be identified (Fig. 7).

of 1.8×0.9 mm^2 yielding a pixel resolution of 0.88 μm in both directions. The single images are stitched together to create expanded mosaic images of the entire printed structure. Fig. 7 shows a cut-out of such a test structure, a meander with contact pads on both ends. It is printed with silver nano-particle ink onto the Mitsubishi PET substrate at a fixed jetting frequency f_{pmax} of 100 Hz, a print head velocity of 15 mm/s, acceleration of 1500 mm/s^2 and jerk of 15,000 mm/s^3. Already with the naked eye the droplet accumulation when the print head moves at nonconstant velocity is clearly visible at the beginning and end of the lines and the contact pad. Due to the wetting of the ink on the substrate, droplet separation occurs beyond a droplet spacing of about 120 μm. For these regions of the line, droplet centres of gravity and the spacing from one droplet centre to the next are calculated by image processing. Fig. 8 plots the resulting droplet spacing along one line of the meander of Fig. 7.

The acceleration and deceleration phases are clearly reflected in the droplet spacing. Such a nonuniform droplet spacing reduces the quality of printed electronic devices. Thus, in order to synchronise the jetting frequency with the velocity of the print head motion, the piezo print head is defined as virtual stepper axis in addition to the real axes driving the motion system in the Beckhoff TwinCat control of the printing system as outlined in Section 3. However while the axis parameters of the real stepper axes are fixed, the axis parameters of the virtual axis are calculated in the generator tool based on prior knowledge, such as ink type, print head type and ink/substrate interaction. This method allows to include the piezo print head in the path planning of the Beckhoff

NCI module (Fig. 9). The stepper pulses generated by the NCI module for the virtual stepper axis are fed to a Beckhoff EL2521 pulse train terminal (PTT) whose pulse signal is converted to $a + 5$ V trigger signal for the piezo print head controller by means of an adaptor circuit. The generator tool generates G-Code motion commands for the x-, y- and z-axes and the virtual stepper axis. The Beckhoff TwinCat NCI module calculates the path planning over the three real and the "virtual" print head stepper axes and ultimately generates the output to the axes. In the case of the "virtual" print head stepper axis the generated stepper pulses are used to trigger the print head via the pulse train terminal.

Dotted lines are printed as test structures with the same motion parameters as above, with the jetting frequency adapted to the print head velocity by means of the virtual stepper axis with the maximum frequency set to 100 Hz. Thereupon, ink accumulations at the beginning and end of the line are no longer visible to the naked eye. Hence, this structure can be characterised over the entire line length by image processing and the droplet spacing can be calculated with the same method as before.

Table 2 compares the droplet parameters calculated over several test structures printed with the two jetter control methods. Between the two types of test structures, mean droplet size differs by about 6%, mean droplet spacing in the central part differs by about 4%. Moreover, it should be noted, as outlined above, that for the line printed with constant jetter frequency, the beginning and end of the line where the dots merge are excluded for analysis. Despite these limitations, the above results indicate that operation of the jetter as virtual axis significantly reduces droplet spacing variations.

To properly implement this method for the three inks, test suites were performed to investigate ink-print head interaction and ink-substrate interaction. Influencing factors are e.g. rheological properties of the ink, interfacial energies of ink, printing nozzle material and substrate material. From these tests process windows for print head frequency f_p and dot spacing d_{dot} were identified. Depending, on the required structure quality the parameter values were selected for configuration of the piezo print head as virtual stepper axis in the Beckhof control. This approach shall be illustrated with the following example: In order to print the conductor tracks in the demonstrator circuit (Figs. 6 and 13) with 110 μm width the virtual stepper axis parameter d_{dot} (Eq. (2)) is set to 50 μm. The motion system is set to move the piezo print head at a velocity of 10 mm/s (acceleration 1500 mm/s^2, jerk 15,000 mm/s^3). Hence according to Eq. (2) the corresponding virtual stepper axis i.e. piezo print head frequency f_{pmax} is 200 Hz. The print head frequency is ramped up and down in the acceleration and deceleration phases by the
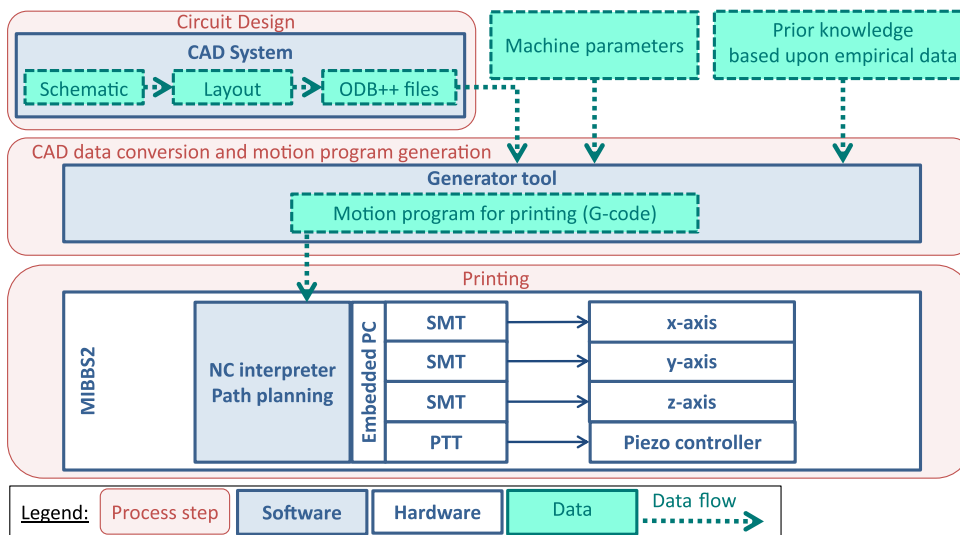
Fig. 9. Integration of the piezo print head "virtual stepper axis" [15].

Table 2
Comparison of droplet spacing measurements.

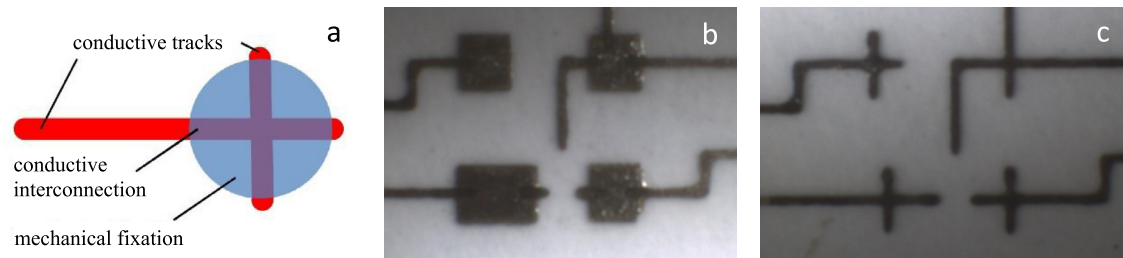|	Constant jetter frequency			Jetter as „virtual stepper axis"		
	Start	Centre	End	Start	Centre	End
Mean droplet size/std. deviation (µm)	103.6 µm/0.8 µm			110.3 µm/3.5 µm		
Mean droplet spacing (µm)	144.1	149.8	144.2	154.9	155.2	155.4
Minimum measured droplet spacing (µm)	124.7	143.9	129.0	147.9	151.1	152.7
Std. deviation (µm)	8.5	2.1	3.8	3.3	1.5	2.0

Fig. 10. (a) Schema of printed bond pad geometry for combined mechanical and electric fixation, additionally applicable as fiducial marks for image processing (b) BF2040 footprint with rectangular pads (c) BF2040 footprint with cross-shaped pads.

Beckhoff TwinCat NCI Module in the same way as the stepper pulses of the motion system axes thus yielding uniform printed lines.

4.3. Mounting of smd components on flexible foil substrates

In Section 2.2.4, different challenges in the adaption of SMD component mounting to flexible substrates are outlined that will be addressed in the following. Fig. 10(a) illustrates the concept of enhancement of SMD component fixation on printed structures with a novel contact pad design on the example of a cross-shaped bond pad. This design provides areas where the conductive adhesive is in contact with the printed conductive track as well as areas where it is in contact with the plain substrate. The conductive adhesive is in the first place a base adhesive with embedded conductive material (flakes, nano particles). Thus, a mechanical connection is established in the area with substrate contact, provided that the base adhesive chemistry matches with the substrate material. In the area of contact with the conductive tracks, the electrical connection is realised. This additional mechanical connection will considerably reduce the risk of delamination of the conductive tracks from the substrate due to weak adhesion. It is evident that this mounting concept can be combined with the above outlined structural adhesive concept for even more enhanced connection stability. Figs. 10(b) and (c) show the original footprint of the BF2040 with printed square bond

pads and the adapted design with cross-shaped bond pads, respectively. Both footprint layouts follow the iterative approach that allows for SMD component assembly as well as for printing of a transistor between the contact pads.

A further challenge is the more precise component positioning. In order to address this challenge, the SMD component mounting process is enhanced by an additional step for the precise positioning of components that are imprecisely supplied. Though mounting of SMD components, flip chips and bare dies on PCBs is state of the art in industrial applications [24,25], its integration in an evaluation set-up is an indispensable step towards realizing functional printed systems and a precondition for automated assembly based upon standard feeders of SMD components such as reels. In our set-up, components are supplied with low positional accuracy in trays. In addition to the automatic positioning of small and less complex SMD components described in [15], the basis for a fully automated assembly process of complex components is established and described in the following.

To start the assembly process, the machine is equipped with substrate and electronic components. Then, the positions of the fiducial marks on the substrate are measured. One challenge hereby is the reflecting surface of the foil substrates. The centre of the fiducial marks is determined by analysing the grayscale image and reducing the noise using binari-
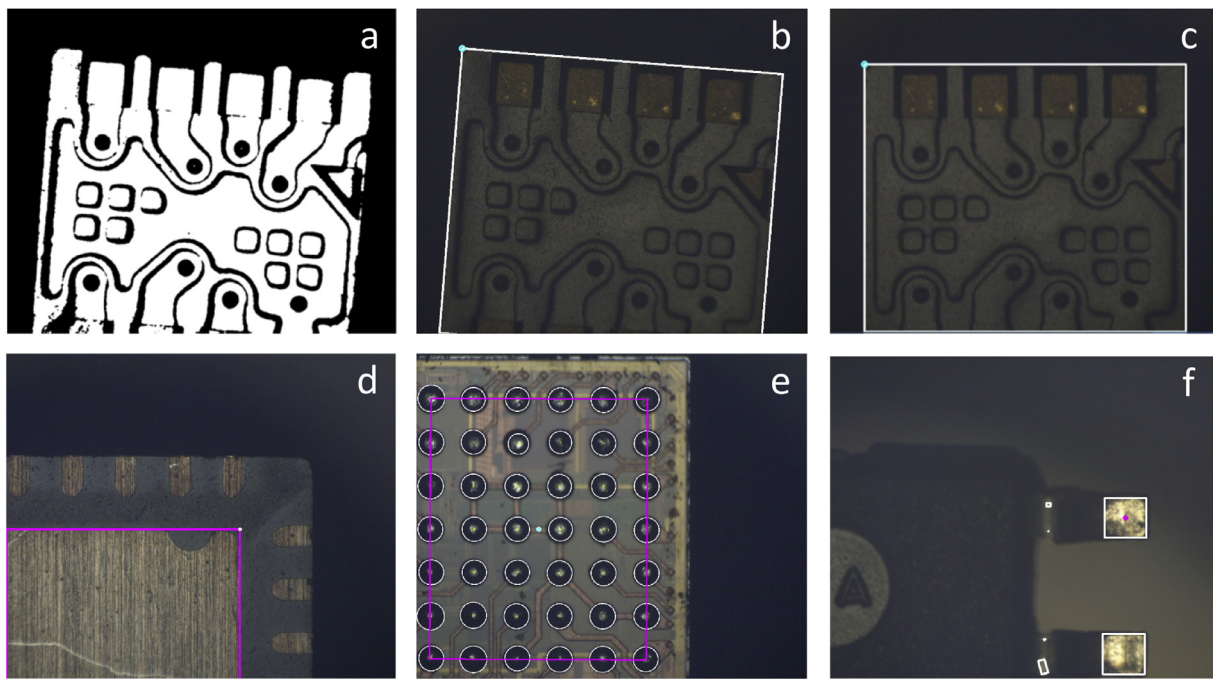
Fig. 11. Images captured by the bottom camera of the MIMOSE system: (a) binarised image generated by image processing (b) extraction of positioning parameters like rotation angle and component position using component identifiers (in this case: smallest circumscribed rectangle) (c) corrected component position (d) thermal pad used as component identifier (e) largest circumscribed rectangle of the ball centres in BGA used as component identifier (f) centre of outer pins used as component identifier.

sation with an adaptive threshold. After a morphologic transformation, the circle is found with the help of a Canny edge detector and a Circle Hough transform [41,42].

After calibration and adhesive application, the mounting process begins by picking up the component with a vacuum tool and capturing an image from below with the bottom camera. The image processing steps consist of the subtraction of the background image, contrast amplification by normalizing the captured greyscale values to the entire spectrum of greyscale values and bilateral filtering. In order to create a binary image (Fig. 11(a)), a threshold value is determined automatically. Then, the identifiers for the respective component are acquired, e.g. the smallest circumscribed rectangle of the component outline (Fig. 11(b)). Subsequently, the component angle and lateral position are determined. The rotation angle is corrected (Fig. 11(c)) and the component can be placed into the final mounting position. For correction of the rotation angle of components, it has to be considered, that the centre of the component and the axis of rotation do not coincide. There are two reasons: the gripper tool is mounted eccentrically in the machine and frequently the gripping position does not exactly match the centre of the component due to imprecise feeding in the magazine. Therefore, a transformation of the respective positions is necessary.

Depending on the type and size of the components, different methods are applied for the acquisition of the component identifiers. For small and less complex SMD components which can be captured by the field of view of the camera, the smallest circumscribed rectangle is identified whose centre and angle are used. The positional uncertainty of the component on the gripper based on the image processing is approx. ±20 μm [15]. The same method is applied for components larger than the field of view. For QFN packages (Quad Flat No-Lead) or comparable components, the thermal pad at the bottom including a special fiducial mark for positioning is used. For BGAs (Ball Grid Arrays), the balls are detected using the Circle Hough Transform. Then, the largest circumscribed rectangle of the ball centres is determined. It has to be guaranteed by the positioning of the component above the camera, that at least two border rows of balls are captured in the field of view. For components with pins

without significant bottom fiducial marks exceeding the field of view, like Small Outline Integrated Circuit (SOIC) or Thin Shrink Small Outline Package (TSSOP), first the top camera is used to roughly acquire the angle of the component. Then, two images are captured of the outer diagonal pins with the bottom camera. Using the centre of these pins and the information on the component shape, the centre of the component can be calculated. Figs. 11(c)-(f) show the application of the described image processing methods for respective examples of component positioning.

4.4. Measurement of substrate warpage by deflectometry

In order to validate applicability of deflectometry measurement for detection of substrate warpage, a pristine 200×200 mm^2 sheet of Dupont Melinex ST 506 was subjected to a typical oven process for thermal sintering of the silver nano-particle ink with a temperature of 120 °C for one hour. Fig. 12 shows the substrate surface before and after the oven process reconstructed from deflectometry measurements.

This example indicates that this measurement principle can be applied to detect substrate warpage. Furthermore, it illustrates that already pristine, unprinted substrates have an embedded strain that can lead to significant warpage. Therefore, either special clamping or adjustment of the print head distance to the substrate surface is required during the printing process.

4.5. Final printed, hybrid integrated demonstrator circuit

Fig. 13 shows the final printed demonstrator circuit realised by the application of the improved automated workflow. The circuit comprises the printed structures wiring, resistors, plate capacitors and crossconnects as well as transistors mounted as SMD tetrodes. It proves to be functional with an audible output at the piezo buzzer. The new approach for integrating the piezo print head as a virtual stepper axis in the path planning yields highly precise vector printing. This control strategy allows to print resistor values with a standard deviation of resistance
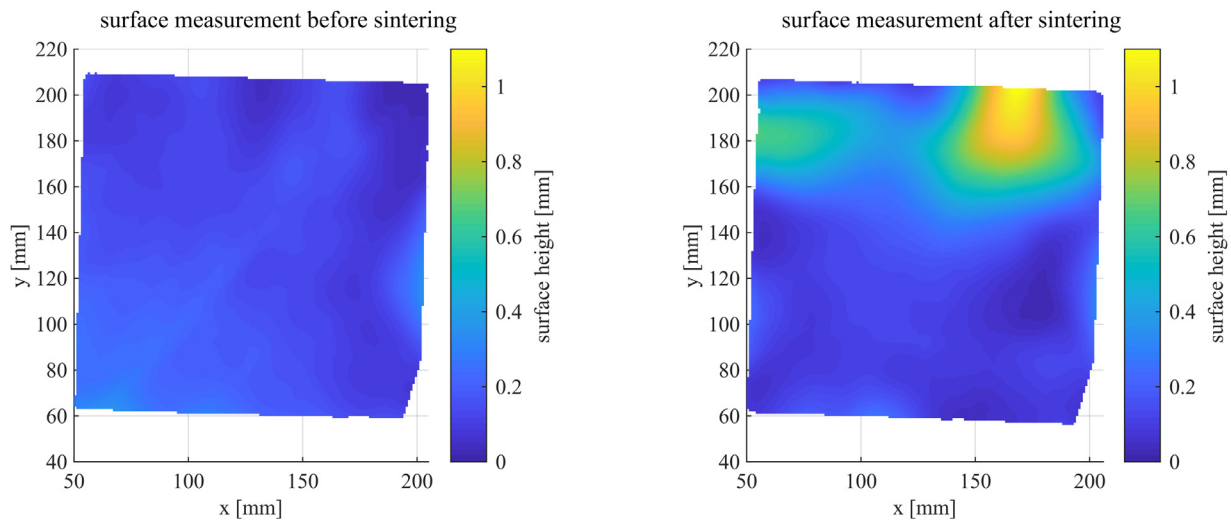
Fig. 12. Substrate surface before and after sintering, the depth map is reconstructed from deflectometry measurements.
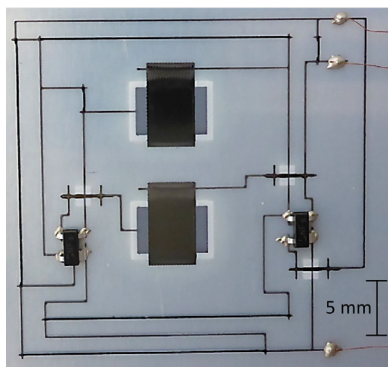
Fig. 13. Printed, hybrid integrated demonstrator circuit [15].

below 5%. The enhanced mounting techniques for SMD components significantly improve mechanical fixation.

However process yield was identified as serious issue. In the first step of the process chain (see Fig. 6) the wiring of fifty circuits was printed. After every step the results were inspected and the known good circuits were forwarded to the next process step. In the end after all printing, postprocessing and SMD component mounting steps there remained a single fully functional circuit. It oscillated with a frequency of 415 Hz reasonably close to the target frequency of 425 Hz (see 2.2.6) to drive the piezo buzzer. This simple demonstrator circuit already illustrates that in the same way as in conventional electronics the longer the process chain, the more severe yield issues become.

5. Conclusions

A digital workflow for fabricating hybrid printed electronic circuits is presented. The method to automatically generate fabrication programs from a CAD circuit layout proves particularly useful both for fabricating test vehicles and for multistage printing and component mounting processes. Improving the printing process by integrating a piezo print head as a "virtual stepper" axis improves homogeneity of droplet spacing on the substrate. This enables the direct printing of resistors with low tolerances of the resistor values. As complementary process to realise more complex electronic circuits (e.g. integrated micro-controllers) by means of hybrid printed circuits, surface mount technology is adapted to the challenges of foil substrates. New solutions for improving electrical connection and mechanical fixation of SMD components on printed struc-

tures are introduced. Moreover, solutions are implemented to better cope with positional uncertainties during the mounting process. Based upon the envisaged results of systematic investigations of shrinkage in the x-y-plane as well as warpage resulting from postprocessing steps, adjustments have to be implemented into the mounting process. Homogeneous deformation can be compensated by acquiring the positions of a small number of fiducial marks at the substrate corners by means of image processing and determining the real component set-down position using a mathematical model of foil deformation. For inhomogeneous deformations, e.g. caused by ink accumulations, a more elaborate approach is necessary. Local fiducial marks will be used to identify the respective position of each electronic component. For this purpose, a cross-shaped pad design is proposed to be utilised as additional fiducial mark, thereby saving design space.

Furthermore, image processing methods are developed to cope with deformations of the foil substrate during the circuit fabrication process due to embedded strain. First results already allow identification of deformations of pristine substrates by deflectometry. It is to be expected that printed substrates with layout dependant non-uniform ink coverage over larger areas such as in a printed capacitor or a ground-plate aerial will exhibit even more non-uniform warpage. The non-uniform reflectivity of the foil substrate due to the printed features has to be taken into account in image processing. Moreover, systematic effects of the set-up such as a non-ideally planar surface of the pattern generator may have a significant impact on the measurement results. Thorough investigations on these influences on measurements in the present application are attractive topics for future research.

All these measures enhance printing precision, component placement precision and robustness of hybrid printed electronics circuits and thus circuit reliability. For higher integrated hybrid printed circuits with smaller device features and reliable mounting of small pitch flip-chips or bare dies further work is required.

In sum, with the introduced workflow, the basis for automated fabrication of hybrid printed electronic circuits is established. Nevertheless, a lot of groundwork has to be done to realise the full potential of hybrid printed electronics. Process yield remains a significant challenge in fabricating complex electronic circuits with multiple printing steps, several inks and component mounting. In future work, therefore, methods have to be developed which increase process stability and reliability on every stage of the design and fabrication process in order to achieve reasonable yield numbers. Moreover due to the observed influence of environmental conditions, in particular humidity, on circuit performance in operation, another future focus of research lays on the encapsulation of printed circuits [39].

Declaration of Competing Interest

The authors declare that they have no known competing financial interests or personal relationships that could have appeared to influence the work reported in this paper.

CRediT authorship contribution statement

Ulrich Gengenbach: Conceptualization, Resources, Writing - original draft, Writing - review & editing, Visualization, Supervision, Project administration, Funding acquisition. **Martin Ungerer:** Conceptualization, Methodology, Validation, Investigation. **Liane Koker:** Conceptualization, Methodology, Validation, Writing - original draft, Writing - review & editing, Visualization. **Klaus-Martin Reichert:** Methodology, Software, Validation, Investigation, Resources, Data curation, Visualization. **Peter Stiller:** Methodology, Software, Validation, Formal analysis, Data curation, Writing - review & editing. **Stephan Allgeier:** Methodology, Validation, Formal analysis, Investigation, Writing - original draft, Visualization, Writing - review & editing. **Bernd Köhler:** Conceptualization, Methodology, Writing - review & editing, Supervision, Project administration. **Xiaoqi Zhu:** Software, Validation, Investigation. **Chengyuan Huang:** Software, Validation, Investigation. **Veit Hagenmeyer:** Writing - review & editing, Supervision, Funding acquisition.

Funding

References

[1] Chang JS, Facchetti AF, Reuss R. A circuits and systems perspective of organic/printed electronics: review, challenges, and contemporary and emerging design approaches. IEEE Journal on emerging and selected topics in circuits and systems 2017;7(1):7–26.

[2] Schwartz DE, Rivnay J, Whiting GL, Mei P, Zhang Y, Krusor B, et al. Flexible hybrid electronic circuits and systems. IEEE Journal on emerging and selected topics in circuits and systems 2017;7(1):27–37.

[3] Saengchairat N, Tran T, Chua CK. A review: additive manufacturing for active electronic components. Virtual Phys Prototyp 2017;12(1):31–46.

[4] Garlapati SK, Divya M, Breitung B, Kruk R, Hahn H, Dasgupta S. Printed Electronics Based on Inorganic Semiconductors: from Processes and Materials to Devices. Advanced Materials 2018;30(40) Art. Nr.: 1707600.

[5] Wu W. Inorganic nanomaterials for printed electronics: a review. Nanoscale 2017;9(22):7342–72.

[6] Kipphahn H. Handbook of print media. Springer; 2014.

[7] Derby B. Inkjet Printing of Functional and Structural Materials: fluid Property Requirements, Feature Stability, and Resolution. Annu Rev Mater Res 2010;40(1):395–414.

[8] Cui Z. Printed electronics: materials, technologies and applications. John Wiley & Sons; 2016.

[9] Nisato G, Lupo D, Ganz S, editors. Organic and printed electronics. New York: Jenny Stanford Publishing; 2016.

[10] Schneiderman R. Modern standardization: case studies at the crossroads of technology, economics, and politics. Wiley; 2015.

[11] Rasheed F, Golanbari MS, Marques GC, Tahoori MB, Aghassi-Hagemann J. A Smooth EKV-based DC Model for Accurate Simulation of Printed Transistors and their Process Variations. IEEE Trans Electron Devices 2018;65(2):667–73.

[12] Oktavianty O, Kyotani T, Haruyama S, Kaminishi K. New actuation waveform design of DoD inkjet printer for single and multi-drop ejection method. Additive Manufacturing 2019;25:522–31.

[13] Ungerer M, Spomer W, Wacker I, Schröder R, Gengenbach U. A Method for the Analysis of the Nano- and Micromorphology of Printed Structures on Flexible Polymer Films. International Journal on Advances in Intelligent Systems 2017;10:382–92.

[14] Kim S, Won S, Sim GD, Park I, Lee S-B. Tensile characteristics of metal nanoparticle films on flexible polymer substrates for printed electronics applications. Nanotechnology 2013;24(8):085701.

[15] Gengenbach U, Ungerer M, Koker L, Reichert K-M, Stiller P, Huang C, Hagenmeyer V. Automated fabrication of multi-layer printed electronic circuits using a novel vector ink-jet printing process control and surface mounting of discrete components. IFAC-PapersOnLine 2019;52(15):609–14.

[16] Mikolajek M, Friederich A, Kohler C, Rosen M, Rathjen A, Krüger K, et al. Direct Inkjet Printing of Dielectric Ceramic/Polymer Composite Thick Films. Adv Eng Mater 2015;17(9):1294–301.

[17] ODB++ Translators and Processors for ODB++, http://www.artwork.com/odb++/odb++_overview.htm [accessed 03.03.2018].

[18] Gengenbach U, Ungerer M, Aytac E, Koker L, Reichert K-M, Stiller P, Hagenmeyer V. An Integrated Workflow to Automatically Fabricate Flexible Electronics by Functional Printing and SMT Component Mounting. 14th IEEE International Conference on Automation Science and Engineering (CASE) Munich; 2018. Paper ThCT4.4.

[19] Deo N. Graph theory with applications to engineering and computer science. Englewood, New Jersey: Prentice-Hall; 1974.

[20] Applegate DL, Bixby RM, Chvátal V, Cook WJ. The traveling salesman problem. Princeton University Press; 2006.

[21] Otten R, Van Ginneken L. The annealing algorithm. Springer US; 1989.

[22] Sun Z-G, Teng H-F. An ant colony optimization based layout optimization algorithm. In: TENCON '02. Proceedings. IEEE Region 10 Conference on Computers, Communications, Control and Power Engineering, 1; 2002. p. 675–8.

[23] Dorigo M, Gambardella LM. Ant colonies for the travelling salesman problem. In: BioSystems, 43. Elsevier; 1997. p. 73–81.

[24] Oakes I. Management of electronics assembly: design, development, production, test. Butterworth-Heinemann; 1992.

[25] Ko KW, Kima JW, Cho HS, Jin KS, Koh KI. Enhancement of Placement Accuracy for SMD via Development of a New Illumination System. In: Proceedings SPIE 2001; 2001. p. 4190. Optomechatronic Systems.

[26] Harper CA. Electronic packaging and interconnection handbook. McGraw–Hill; 2007.

[27] Joo S, Baldwin DF. Adhesion mechanisms of nanoparticle silver to substrate materials: identification. Nanotechnology 2009;21(5) IOP Publishing Ltd.

[28] Krammer O, Illyefalvi-Vitéz Z. Investigating the self-alignment of chip components during reflow soldering. Periodica Polytechnica Electrical Engineering (Archives) 2008;52(1–2):67–75.

[29] Baby TT, Cadilha Marques G, Neuper F, et al. Printing Technologies for Integration of Electronic Devices and Sensors Functional nanostructures and sensors for cbrn defence and environmental safety and security nato science for peace and security series C: environmental security. Sidorenko A, Hahn H, editors. Dordrecht: Springer; 2020.

[30] Gengenbach U. Automatic assembly of micro-optical components. International Society for Optics and Photonics (SPIE); 1996. p. 141–50.

[31] Huang L, Idir M, Zuo C, Asundi A. Review of phase measuring deflectometry. Opt Lasers Eng 2018;107:247–57.

[32] Knauer MC, Kaminski J, Häusler G. Phase measuring deflectometry: a new approach to measure specular free-form surfaces. In: Proceedings SPIE 2004, 5457; 2004. p. 366–76.

[33] Faber C. New methods and advances in deflectometry. Erlangen Scientific Press; 2012.

[34] Allgeier S, Gengenbach U, Köhler B, Reichert K-M, Hagenmeyer V. Robust phase unwrapping based on non-coprime fringe pattern periods for deflectometry measurements. In: Proceedings SPIE 2019, 11061; 2019.

[35] Koker L, Ungerer M, Mikolajek M, Neuper F, Kühner T, Gengenbach U. Data-driven Design of an Inkjet-Printed Electronic Circuit. LOPEC 2018 M u nich; 2018. oe-a.

[36] Jung S, Sou A, Gili E, Sirringhaus H. Inkjet-printed resistors with a wide resistance range for printed read-only memory applications. Org Electron 2013;14:699–702.

[37] Mikolajek M, Reinheimer T, Bohn C, Kohler C, Hofmann MJ, Binder JR. Fabrication and Characterization of Fully Inkjet Printed Capacitors Based on Ceramic/Polymer Composite Dielectrics on Flexible Substrates. Sci Rep 2019;9:13324.

[38] Reinheimer T, Azmi R, Binder JR. Polymerizable Ceramic Ink System for Thin Inkjet-Printed Dielectric Layers. ACS Appl. Mater. Interfaces 2020;12:2974–82.

[39] Chen Z, Mansour M, Gengenbach U, Koker L. Approaches for Solution-Processed Encapsulation of Printed Medical Wearable Devices. Current Directions in Biomedical Engineering 2020 submitted paper.

[40] Duineveld P. The Stability of Ink-Jet Printed Lines of Liquid with Zero Receding Contact Angle on a Homogeneous Substrate. J Fluid Mech 2003;477:175–200.

[41] Canny J. A Computational Approach to Edge Detection. IEEE Trans Pattern Anal Mach Intell 1986;PAMI-8:679–98.

[42] Duda RO, Hart PE. Use of the Hough transformation to detect lines and curves in pictures. Commun ACM 1972;15(1):11–15.

PD Dr.-Ing. Ulrich Gengenbach is head of research area System integration for Nano and Micro Systems at the Institute for Automation and applied Informatics (IAI) at Karlsruhe Institute of Technology (KIT), Germany. His research interests are "Design-for-X" and integration technologies.

Martin Ungerer is a researcher at the Institute for Automation and Applied Informatics (IAI) at Karlsruhe Institute of Technology (KIT), Germany. His-research interests are printing technologies and printed systems.

Dr.-Ing. Bernd Köhler is a team leader and a project manager at the Institute for Automation and Applied Informatics (IAI) at the Karlsruhe Institute of Technology (KIT), Germany. His-research interests are automated inspection of microstructures and image processing.

Dr.-Ing. Liane Koker is a researcher at the Institute for Automation and Applied Informatics (IAI) at Karlsruhe Institute of Technology (KIT), Germany. Her research interests are system integration of printed systems and medical applications.

Xiaoqi Zhu is an engineer who contributed to this paper in the context of his master thesis at the Institute for Automation and Applied Informatics (IAI) at Karlsruhe Institute of Technology (KIT), Germany. His-focus of activity is automatic control in fluid system. He is now working in an industrial company.

Klaus-Martin Reichert is an engineer at the Institute for Automation and applied Informatics (IAI) at Karlsruhe Institute of Technology (KIT), Germany. His-focus of activity is software development and application.

Chengyuan Huang is an engineer who contributed to this paper in the context of his master thesis at the Institute for Automation and Applied Informatics (IAI) at KIT. He is currently with Sichuan Jeshine Medical CO., Ltd and working on the development of medical devices.

Peter Stiller is a mathematician at the Institute for Automation and applied Informatics (IAI) at Karlsruhe Institute of Technology (KIT), Germany. His-focus of activity is software development.

Prof. Dr. Veit Hagenmeyer is director of the Institute for Automation and Applied Informatics (IAI) at Karlsruhe Institute of Technology (KIT), Germany. His-main fields of work are automation technology, control engineering, mechatronics and energy informatics.

Dr.-Ing. Stephan Allgeier is a researcher at the Institute for Automation and Applied Informatics (IAI) at Karlsruhe Institute of Technology (KIT), Germany. His-research interests are image processing algorithms with a focus on biomedical imaging and automated inspection applications. He currently researches techniques for topography measurements for transparent materials using deflectometric approaches.